Cleaner Materials 3 (2022) 100043

Contents lists available at ScienceDirect

Cleaner Materials

journal homepage: www.elsevier.com/locate/clema

Reactivation of alkali-activated materials made up of fly ashes from a coal power plant

M. Criado [a,*], M. Vicent [b], F.J. García-Ten [b]

[a] Department of Construction, Instituto de Ciencias de la Construcción Eduardo Torroja-CSIC, c/Serrano Galvache 4, 28033 Madrid, Spain
[b] Instituto de Tecnología Cerámica (ITC), Asociación de Investigación de las Industrias Cerámicas (AICE), Campus Universitario Riu Sec (UJI), Avda. de Vicent Sos Baynat s/n, 12006 Castellón, Spain

ARTICLE INFO

Keywords:
Alkali-activated materials
Fly ash
Circular economy
Reactivation

ABSTRACT

Fly ash, generated during the combustion of coal for producing energy, is an industrial by-product that is suitable as starting material for the synthesis of alkali-activated materials due to its amorphous aluminosilicate content that is a mandatory requirement for obtaining materials with improved mechanical properties.

According to the circular economy concept and taking into account some specific issues such as waste circularity, that provides environmental and societal benefits, this work proposes the successive alkaline activation processes of already alkali-activated materials with the purpose of being recovered several times, contributing to the sustainability of the construction materials.

In this work, alkali-activated materials have been prepared using fly ash as starting waste material during successive activations, maintaining constant the alkaline activator and modifying the liquid/solid ratio according to the workability of the mixtures. The materials obtained have been fully characterised. A mineralogical and microstructural study of these materials was conducted by FTIR, XRD, and ESEM-EDX. Moreover, it has been determined their bulk density, strength resistance, open porosity and efflorescence formation, confirming their suitability for being used in a second activation.

Introduction

The objectives and targets set up in the environmental European legislation have been key drivers to improve waste management, stimulate innovation in recycling, limit the use of landfilling and create incentives to change consumer behaviour. In this sense turning waste materials from one industry into a resource for another is one key towards a circular economy, as resources are used more efficiently and sustainably ("Environment Action Programme to 2020. Environment Policies. Waste", 2020).

Improving waste management also helps to reduce health and environmental problems, reduce greenhouse gas emissions (directly by cutting emissions from landfills and indirectly by recycling materials which would otherwise be extracted and processed) and avoid negative impacts at a local level such as landscape deterioration due to landfilling, local water and air pollution, as well as littering ("Environment Action Programme to 2020. Environment Policies. Waste", 2020). For the European Commission, the circularity of materials is so a critical issue that on 16 January 2018 released a set of indicators to monitor the progress towards the circular economy ("European Commission. Eurostat. Manuals and Guidelines. Circular material use rate CALCULATION METHOD 2018 edition", 2018). Among these indicators, note that the 'circular material use rate' measures the contribution of recycled materials to the overall raw materials used to manufacture a product ("European Commission. Eurostat. Products Datasets", 2021).

The production of electrical energy from thermoelectric plants that use coal (pulverised anthracite or other bituminous carbons) as fuel, leads to different types of by-products. Various terms have been used to describe coal combustion products (CCPs). Terms including coal ash, pulverised fuel ash, coal utilisation by-products (CUBs), coal combustion by-products (CCBs), coal combustion residues (CCRs), coal combustion waste materials and others are used to describe what are basically the same materials. CCPs are produced in huge amounts (2016 annual production is 1221.9 Mt (Harris et al., 2019)) and can become a secondary raw material for other products. These other products include, but are not limited to, cement and concrete, structural filler and covering material, roadway and pavement utilisation, addition to construction materials as a lightweight aggregate, infiltration

* Corresponding author.
E-mail address: maria.criado@ietcc.csic.es (M. Criado).

https://doi.org/10.1016/j.clema.2022.100043
Received 19 October 2021; Revised 13 December 2021; Accepted 3 January 2022
Available online xxxx

barrier and underground void filling, and soil, water and environmental improvement (Ahmaruzzaman, 2010).

The action of firing coal leads fundamentally to fly ash and bottom ash, whose main difference is the size of the particles. The finer particles (fly ash) is obtained by mechanical or electrostatic precipitation of suspended dust in the combustion gases (about 80%, by weight), while the coarser (bottom ash) fall to the bottom by gravity (about 20%, by weight) (Gikunoo et al., 2005).

Fly ash is generally grey in colour, abrasive, mostly alkaline, and refractory in nature (Rogoff and Screve, 2019). It is defined as a fine powder with mainly spherical particles, which has pozzolanic properties and is composed mainly of SiO_2 and Al_2O_3 ("EN 450-1, 2006). The amount of crystalline and glassy phase depends largely on the combustion and gasification process used at each power plant (Fernández-Jiménez et al., 2008).

There are essentially four basic benefits associated with fly ash valorisation: immobilisation of metals, cost-effective management, conservation of natural resources and conservation of landfill capacity. The first and most important goal is to immobilise metals (Cu, Ni, Pb, Zn, Cr, Cd…) contained in the fly ash (Darmayanti et al., 2019; Vu and Gowripalan, 2018; Xia et al., 2019) so that any utilisation option is environmentally safe. Apart from that, the economic advantage of avoiding landfilling costs that can reach tens or hundreds of euros per ton, depending on the type of landfill used and on the country, has to be considered (Rogoff and Screve, 2019).

Alkali-activated materials are cold-setting binders made by alkaline activation of reactive aluminosilicate materials to form an "aluminosilicate network". Several materials or waste ones (including fly ash) display this reactivity because they contain a glassy phase with certain quantities of silica and alumina (Fernández-Jiménez et al., 2005). The reaction mechanism of alkali-activated materials can be described in two steps that are partially overlapped (Buchwald et al., 2009):

1. Dissolution of the glassy phase, in which the alkaline solution breaks down the solid network of the glass to produce small reactive silicate and aluminate species.

2. Condensation of these monomers and oligomers, thus forming an aluminosilicate network in which sodium and water are inserted in the structure.

In the specific case of activating fly ash in an alkaline media, a material with high mechanical strength is formed. The presence of small quantities of zeolites forming part of the cementitious material is also detected (Fernández-Jiménez et al., 2006a). Due to its improved mechanical properties, there is significant literature focusing on the study of alkaline activation of fly ashes (Chi, 2015; Ma et al., 2017; Ruengsillapanun et al., 2021; Škvára et al., 2009) and even fly-ash mixtures (Mardani-Aghabaglou et al., 2014; Yousefi Oderji et al., 2019). In addition, recent studies (Xiao et al., 2021, 2020) have been carried out using thermodynamic simulation to predict the phase assemblages of alkali-activated materials and gain insights into the designing of aluminosilicate precursors. However, no papers in the scientific literature were found in which the valorisation of already alkali-activated materials has been studied.

In this work, fly ash has been used as starting material to obtain alkali-activated specimens which were ground, milled and subjected to successive activations (3 in total) for obtaining new specimens to determine the circularity of these types of materials. In this way, alkali-activated materials could be recovered several times at the end of their service life, once buildings and structures have been demolished, and thus contribute to more sustainable construction.

The fly ash used in this work was fully characterised by chemical and mineralogy methods, including the determination of the potential silica and alumina reactivity. The specimens obtained were characterised in depth by using infrared spectroscopy (FTIR), X-ray diffractometry (XRD) and environmental scanning electron microscopy (ESEM). Moreover, mechanical strength, compacity, open porosity and efflorescence tests were carried out to determine the technological properties.

Experimental

Starting materials

Spanish fly ash (Carboneras, Almería) was the waste material used in this study as binder material. The as-received fly ash was sieved to obtain a fraction below 100 μm for conducting the tests in order to avoid coarse granules or agglomerates.

The alkaline solution, with a SiO_2/Na_2O weight ratio of 0.2, was made up of 85% of sodium hydroxide and 15% of sodium silicate. Sodium hydroxide solution was NaOH 10 M from PANREAC (40% w/v for analysis) with a density of 1.33 g/cm^3. Na_2SiO_3 solution or waterglass from MERCK had the following specifications:

- $3SiO_2{\cdot}Na_2O$ (M = 242.3 g/mol).
- Weight composition: 25.5–28.5% SiO_2 and 7.5–8.5% Na_2O.
- Density: 1.296–1.396 g/cm^3 at 20 °C.

Preparation of the alkali-activated mixtures

The procedure employed for preparing the mixtures is described as follows and the nomenclature of the mixtures tested is defined in Table 1. The starting fly ash sieved at 100 μm (FA0) was mixed with the activating solution at a liquid/solid (l/s) ratio of 0.40. After the mixing, the paste was poured into 80 × 20 × 7 mm prismatic moulds, cured at 85 °C and 95% relative humidity for 20 h and finally demoulded. These alkali-activated specimens were referred to as FA1. A great amount of FA1 specimens were prepared because part of them (10 specimens) were fully characterised and the rest were milled for studying the reactivation process. For that purpose, 100 g of FA1 specimens were wet grounded in an alumina planetary ball mill (MILL-2, Gabbrielli, srl, Italy) with distilled water with a solids content of 70% for 25 min at 410 rpm. After that, the material was dried below infrared lamps and the dry powder was de-agglomerated in a centrifugal laboratory crusher (Model 10000, Orto Alresa, Spain).

Before the reactivation process, FA1 powder was sieved at 100 μm and then was activated again with the same activating solution but using a different l/s ratio, in this case, it was 0.43. Subsequently, the samples were cured following the same procedure described previously. The specimens obtained were referred to as FA2.

Some FA2 specimens were also characterised while others were grounded and sieved at 100 μm again. This procedure was repeated once more time. In this last case, the l/s ratio was 0.55 and the alkali-activated samples obtained were referred to as FA3. It is important to note that the l/s ratio has been modified in order to maintain constant workability in all the pastes.

Characterisation of the starting powder, the alkali-activated specimens and the reactivated powders

The chemical composition of the starting fly ash and the powders obtained after each activation were chemically characterised by Wavelength Dispersive X-Ray Fluorescence, WD-XRF, in a spectrometer with Rh tube and 4 kW power (Axios, PANalytical, The Netherlands) and

Table 1
Alkali-activated trials.

Powder references	l/s ratio	Alkali-activated specimen references
FA0	0.40	FA1
FA1	0.43	FA2
FA2	0.55	FA3
FA3	–	–

using reference materials that guarantee the traceability of the measurements. For that purpose, the samples were previously prepared as fused beads and pressed powder pellets. To prepare the fused beads, the samples were mixed with a mixture of $LiBO_2/Li_2B_4O_7$ as a flux in a Pt/Au crucible, adding a solution of LiI as a bead-releasing agent. The mixture was then subjected to the fusion process in an automatic fusion bead preparation machine (Perl X'3, Philips, The Netherlands). The pressed powder pellets were prepared by using a solution of n-butyl methacrylate in acetone as a binder and they were formed in a hydraulic press (custom-made, Casmon, Spain).

Thermo-gravimetric analysis, TGA (SDT Q600, TA instrument, USA), was used to identify the mass loss of the samples. For this, 25 mg of powdered sample were heated from 30 to 1000 °C at a heating rate of 10 °C/min, under nitrogen flowing atmosphere.

The quantification of the potential reactivity of the original fly ash and the reactivated materials obtained from the first and second activations were determined by an acid attack (Fernández-Jiménez et al., 2019; UNE 80225, 2012). For this, 1 g of sample was placed in 100 mL of HF solution (1%) for 5 h. The resulting solution was filtered, neutralised, and then analysed to determine the amount of silica and alumina dissolved, i.e. the potentially reactive oxides, by Inductively Coupled Plasma Atomic Emission Spectroscopy (ICP-AES, Varian 625, Australia). The tests were conducted with a power of 1.20 kW, a plasma gas flow of 15.00 L/min, an auxiliary gas flow of 1.50 L/min, a nebuliser gas flow of 0.75 L/min and a reading time of 6 s.

Moreover, the rejection of 63 μm of all powders ($d < 100$ μm) was determined by wet sieving in order to obtain information related to particle size distribution.

The colour parameters (L*, a*, b*) of the original fly ash and the alkali-activated powders after each activation were also determined by a diffuse reflectance spectrophotometer (Color-Eye® 7000A, Macbeth/X-Rite, USA). The powder was manually compacted in a capsule with an optical glass bottom, avoiding the formation of cracks in the surface in contact with the glass. One preparation was made, four measurements being taken of each, turning the capsule approximately 90° between every two successive measurements. The measurement conditions were as follows: CIE D65 standard illuminant, CIE 10° standard observer, ultraviolet component excluded, and specular component excluded.

The original fly ash and the alkali-activated materials after each activation were characterised by X-ray diffraction (XRD), Fourier-transform infrared spectroscopy (FTIR), and environmental scanning electron microscopy (ESEM/EDX). XRD (D8 Advance instrument, Bruker, Germany) with Cu-Kα radiation and a nickel filter. The tests were conducted with a nominal step size of 0.02° and a counting time of 0.5 s/step, from 2θ angles 5° to 60°. FTIR (Thermo Scientific Nicolet 6700, USA). The samples were prepared by mixing 200 mg of KBr and 1 mg of the powdered sample. Spectral analysis was performed over the range 4000–400 cm^{-1} at a resolution of 4 cm^{-1} (64 scans). ESEM (S-4800, Hitachi, Japan) equipped with an energy dispersive analyser, EDX (5030, Bruker, Germany). EDX analyses were done with an accelerating voltage of 20 kV, a working distance of 15 mm, and a beam current of 20 μA. An average of 50 analyses was taken per sample.

The bulk density of the specimens was determined by the mercury immersion method after 24 h. Most of the methods used to determine the bulk density consist of weighing the sample and calculating its volume based on Archimedes' principle, i.e. determining the weight of the volume of the liquid displaced by the sample. The mercury immersion method is based on this principle, and it is commonly used in the ceramic industry.

Three-point bending strength of the specimens was conducted in a mechanical testing machine (CM-C, Hoytom, S.L., Spain) at a constant deformation speed of 5 mm/min after 24 h. 10 specimens of each sample were tested.

Open porosity was assessed as water absorption after 24 h. This property was calculated by measuring the weight gain undergone by the specimens after being subjected to a vacuum pressure of 91 kPa for 30 min and subsequently immersed in water for a period of 15 min.

The tendency to efflorescence formation has been determined visually on specimens that had been kept for 7 days in a device designed to accelerate the salt dissolution and migration to the specimen surface. The device consists of a closed container with distilled water in which one face of the specimens was immersed, while the other face remains exposed to the environment. In this way, the preferential drying of the specimen is forced through one of the faces, in which the salts causing the efflorescence are concentrated.

Results and discussion

Chemical characterisation

Table 2 shows the chemical composition of the original fly ash and the material used for the successive activations. The main oxides detected in the original fly ash were SiO_2, Al_2O_3 and Fe_2O_3. In the successive activations, a progressive reduction of all the elements present in the material was observed, with the exception of Na_2O, which increased significantly. The change in the chemical composition is due on the one hand to the diluting effect exerted by the alkaline solution used, rich in Na_2O, and on the other hand to the components that the alkaline solution contributes to the specimens (Na_2O, SiO_2 and H_2O). Thus, the increase in Na_2O is due to the contribution of sodium in the alkaline solution, which does not, however, increase the proportion of SiO_2 because this oxide is present in the alkaline solution in a lower proportion than in the FA0 composition.

It is interesting to note that while the reduction experimented by some oxides (from FA0 to FA3) such as SiO_2, Al_2O_3 and CaO is in the order of 30%, in other components such as Fe_2O_3, MgO and K_2O it is higher, reaching 60% for the latter.

Finally, a significant increase in calcination loss is detected with successive alkaline activations which may be due to the existence of physically adsorbed water in the sample and which is not totally eliminated at 100 °C, or to the carbonation of the sample by the CO_2 present in the air to form carbonate salts (Na_2CO_3 and/or $CaCO_3$). This fact was verified by measuring the carbonate content by reaction with

Table 2
Chemical composition of the aluminosilicate powders (starting fly ash: FA0; reactivated powders: FA1, FA2 and FA3).

Oxide	Content (by wt%)			
	FA0	FA1	FA2	FA3
SiO_2	55.8	49.5	43.3	39.2
Al_2O_3	21.2	21.1	17.4	14.9
Fe_2O_3	6.65	5.62	4.81	4.35
CaO	3.69	3.57	3.01	2.61
MgO	2.05	1.43	1.17	0.99
Na_2O	0.93	7.8	15.6	18.8
K_2O	2.15	1.19	1.01	0.86
TiO_2	0.94	1.11	0.97	0.83
MnO	0.09	0.05	0.05	0.05
P_2O_5	0.55	0.38	0.32	0.26
BaO	0.23	0.16	0.13	0.11
SrO	0.14	0.13	0.11	0.09
ZrO_2	0.04	0.04	0.04	0.03
ZnO	0.02	<0.01	0.01	0.01
V_2O_5	0.05	0.03	0.03	0.02
Cr_2O_3	0.02	0.02	0.03	0.02
NiO	0.02	0.02	0.01	0.01
SO_3	0.40	0.38	0.32	0.29
Loss of ignition at 1000 °C	4.63	7.48	11.61	16.6

HCl (calcimetry procedure). The CO_2 content determined by the calcimetry procedure was 0.2% for original fly ash (FA0), 2.1% for the samples obtained after the first activation (FA1), 3.8% for the samples obtained after the second activation (FA2) and 3.2% for the samples obtained after the third activation (FA3).

Results are in agreement with the thermogravimetric analysis and the diffractograms of the alkali-activated fly ashes after the second and third activation where a new phase of sodium carbonate, thermonatrite, was observed. However, this is only one of the reasons why the loss of ignition is increasing after every activation.

Samples were exposed to a range temperature of 30 – 1000 ˚C to try to confirm the reason why the loss of ignition increased with the successive activations. Fig. 1 shows the TGA (left axis) and DTG (right axis) results for FA1, FA2 and FA3 samples. TGA and DTG curves suggest three degradation stages for all the samples analysed. In all cases, the massive mass loss (region I) was detected at temperatures below 250 ˚C, with values close to 5.8, 8.8 and 14.1 for FA1, FA2 and FA3, respectively. This weight loss is attributed to the evaporation of the physically absorbed water from the sodium aluminosilicate hydrate gel (N-A-S-H) structure (Ouda and Gharieb, 2021). A second peak at 308 ˚C (region II), corresponds to mass losses of 1.3, 2.9 and 4.9% for FA1, FA2 and FA3 respectively, and is assigned to the evaporation of zeolitic or interstitial water (Mobili et al., 2020). The DTG curves presented a third weight loss, region III, between 500 and 900 ˚C, which may be associated with the decomposition of carbonates (Mobili et al., 2020), with mass losses of 1.7, 2 and 3% for FA1, FA2 and FA3 samples. Therefore, in light of these results, when the number of activations increases, a greater mass loss takes place in the sample when is exposed to temperature due to higher free water and loosely bound water, which is relatively easily evaporated from gel pores and a higher formation of zeolites and sodium carbonates in FA3, confirmed by XRD.

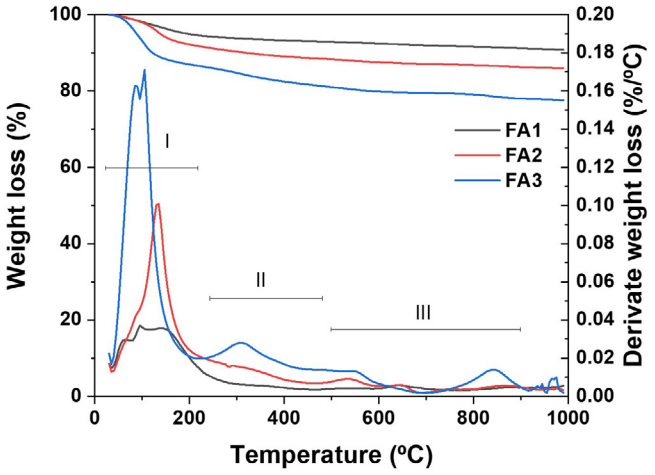

Fig. 1. Thermograms of the alkali-activated samples.

Fig. 2 shows the percentages of potentially reactive silica and alumina identified in the original fly ash (FA0) and in the activated materials (FA1 and FA2). The initial silica and alumina content in the fly ash determined by XRF were 55.8 and 21.2% respectively, these values correspond to the first column of each graph of Fig. 2. The results of the first acid attack (FA0) conducted to determine the ash reactivity demonstrated that all the silica was practically reactive, 97% of total silica, while the reactive alumina content was in the order of 64% of total alumina. This figure also reveals that the reactive potential of the fly ash after the first activation (FA1) decreased due to the fact that the reactive silica and alumina contents were smaller, 46.2 and 8.3% respectively. If these values are compared to the total reactive potential in original fly ash, FA0, the reactive silica was reduced by 15%, and the reactive alumina by 39%. Therefore, some loss of reactive potential of the sample took place after the alkaline activation, which was associated mainly with the decrease of the reactive alumina.

After the second activation (FA2), 6.5% of the reactive alumina was dissolved by acid, while all the bulk silica was reactive, as shown in Fig. 2. The comparison between the reactive potential percentage of the first (FA1) and the second (FA2) alkaline activation showed that the amount of reactive silica was maintained constant, and the percentage of reactive alumina was reduced by 23%. According to the proportion of potentially reactive phases identified by attacking the fly ash after the second activation with acid, this sample should also show low reactivity by decreasing reactive alumina content.

Physical characterisation

Most of the samples of as-received fly ash had a size below 100 μm, which means that only a very little amount of original fly ash (< 2% by weight, determined by dry sieving with a mechanical vibro-sieve shaker) was rejected when it was sieved at 100 μm.

The particle size of the powders to be activated (starting FA0, FA1, FA2 and FA3: all of them with particle size below100 μm) were also assessed by determining the reject on 63 μm (Table 3). The value of the reject is related to the packing behaviour of the powders during the shaping (Sánchez et al., 1998). Therefore, it is assumed that with

Table 3
Reject on 63 μm of activated powders (wt%).

FA0	FA1	FA2	FA3
9.3	2.5	5.4	4.8

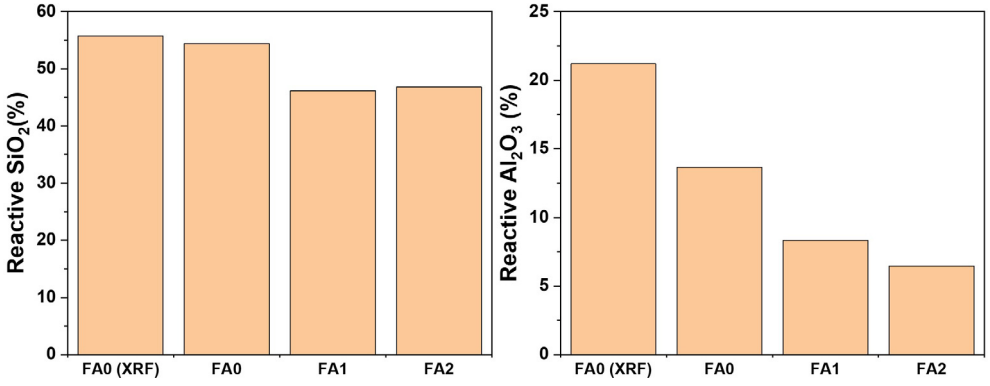

Fig. 2. Potentially reactive silica (left) and alumina (right) of the samples.

the increase of the reject the particle size distribution is wider and will pack better.

Table 4 shows the colour of the original fly ash and reactivated powders, all of them sieved at 100 μm. The measurements were made using the CIELab system of chromatic coordinates, the meaning of which is as follows:

- L*: lightness axis (L* = 100 white, L* = 0 black).
- a*: red to green axis (a* > 0 red, a* < 0 green).
- b*: yellow to blue axis (b* > 0 yellow, b* < 0 blue).

The starting fly ash (FA0), the powder obtained after the first activation (FA1) and the one obtained after the second activation (FA2) have similar grey tonalities. Note that FA0 is a more yellowish powder (highest b*) and FA1 and FA2 are like more whitish-coloured powders (higher L*). After the third activation, the FA3 sample becomes darker (lowest L*) developing a blackish-coloured powder.

Mineralogical and microstructural characterisation

Fig. 3 shows the XRD patterns for the fly ash (FA0) and the alkali-activated powders after the first, second, and third activation (FA1, FA2 and FA3). The diffractogram of the fly ash showed a hump around 15-30°, indicating the amorphous nature of the ash (Criado et al., 2016, 2007; Zerzouri Lakhssassi et al., 2019). The presence of some crystalline phases such as quartz (SiO_2, COD 1011097), mullite ($Al_{4.8}O_{9.6}Si_{1.2}$, COD 7105575), and hematite (Fe_2O_3, COD 9000139) was also confirmed.

In the diffractograms of the alkali-activated samples, independently of the number of activations to which it was subjected, a shift in the thump to slightly higher 2θ values (20-40°) was observed, confirming the formation of a higher content of amorphous reaction product, specifically a sodium aluminosilicate hydrate gel (N-A-S-H) (Criado et al., 2016, 2007; Zerzouri Lakhssassi et al., 2019). The composition of this reaction product depends on the content of potentially reactive phases in the fly ash and the amount of sodium supplied by the alkaline activator in the medium after the activation, as was observed by FTIR and SEM/EDX later on. A higher amount of reactive silica or alumina dissolved lead to the precipitation of rich-Si or rich-Al gel, respectively (Fernández-Jiménez et al., 2019).

A series of diffraction lines on the patterns were observed in these three alkali-activated samples associated with the presence of zeolites. The nature of zeolite depended on the number of alkaline activation processes conducted, i.e. the amount of aluminium and silicon available in the medium. Sodalite ($Al_6H_{0.9}Na_8O_{24.9}Si_6$, COD 1529906) with Si/Al = 1 was detected in the three samples, whose amount increased with the number of activations applied. A new zeolitic phase, zeolite P ($Al_6Na_{5.92}O_{43.28}Si_{10}$, COD 8103734) with Si/Al = 1.67 was formed after the second activation. The gel could consequently be considered a zeolite precursor since certain zeolites are observed in the alkali-activated fly ash cements (Palomo et al., 1999). Therefore, the formation of a zeolite with a higher Si/Al ratio suggested that the main reaction product, N-A-S-H gel, could be richer in silicon, which was confirmed by FTIR and SEM/EDX.

However, after the third activation, the predominant zeolite species were sodalite. These changes can be explained by the fact the zeolites are metastable and may undergo successive transformations into one or several more stable phases. Opened structure zeolites convert to species with a very close structure (Van Bekkum et al., 2001). In the present study zeolite P, a species with a pore size of 0.43 nm, small pore, gave way to zeolite sodalite, which has even a smaller pore size (0.3 nm, very small pore) (Van Bekkum et al., 2001). Besides, after the third activation, the amount of reactive alumina decreased (see Fig. 2) and the amount of available Al to form zeolite P could not be enough (Al/Na ratio ≈ 1) but it was adequate for the synthesis of sodalite (Al/Na = 0.75).

Finally, a new crystalline phase was observed after the second and third alkaline activation, thermonatrite ($Na_2CO_3{\cdot}H_2O$, COD 9011153). An increase in the number of activations induced acceleration in the formation of this compound with an intensification of the diffraction lines at 16.5°, 32.3°, and 37.9° (Husaini et al., 2002), see Fig. 3. The identification of sodium carbonate phases suggests that there is an excess of sodium in the medium. The fly ash was activated with a mix of NaOH and Na_2SiO_3 several times; likely, there is a great amount of sodium dissolved in the system supplied by the alkaline solution, which cannot be consumed with the Al dissolved because the amount of reactive Al has been reduced with the subsequent activations and, as a result, an increase of the soluble alkalis available takes place. When this sodium is in contact with the atmosphere, carbonation occurs and produces thermonatrite (Criado et al., 2005; Hamdane et al., 2020; Ortega-Zavala et al., 2019).

The infrared spectra of the fly ash (FA0) and the alkali-activated powders after the first, second, and third activation (FA1, FA2 and FA3) are shown in Fig. 4. The respective spectra band assignments are summarised in Table 5. All the spectra showed two broad bands around 3444 and 1643 cm^{-1} (peaks 1 and 2) corresponding to the stretching vibration of O–H bond and the bending vibration of H-O–H bonds of water molecules, respectively. In addition, the bands at 1455, 1412, and 866 cm^{-1} (peaks 3, 4, and 9) were attributed to the vibration of the C-O bond of calcium carbonate. Amorphous calcium carbonate and/or small amounts of it were formed; however, they were not detected by XRD. Finally, the presence of quartz gave rise in the spectra to a series of bands located at 1175, 1084, 795–776 (double band), 692, and 460 cm^{-1} (peaks 6, 7, 10, 13 and 17) (Diaz-Loya et al., 2011). While that those attributed to mullite appeared at 1180–1130 cm^{-1} (peak 6, ascribed to the symmetric stretching vibration of Si-O-Si bond) and 560–550 cm^{-1} (peak 16,

Table 4
Chromatic coordinates of the starting fly ash (FA0) and reactivated powders (FA1, FA2 and FA3).

Chromatic coordinates	FA0	FA1	FA2	FA3
L*	51.4	57.1	53.4	38.9
a*	0.6	−0.1	−0.1	0.3
b*	7.8	3.9	2.4	3.1

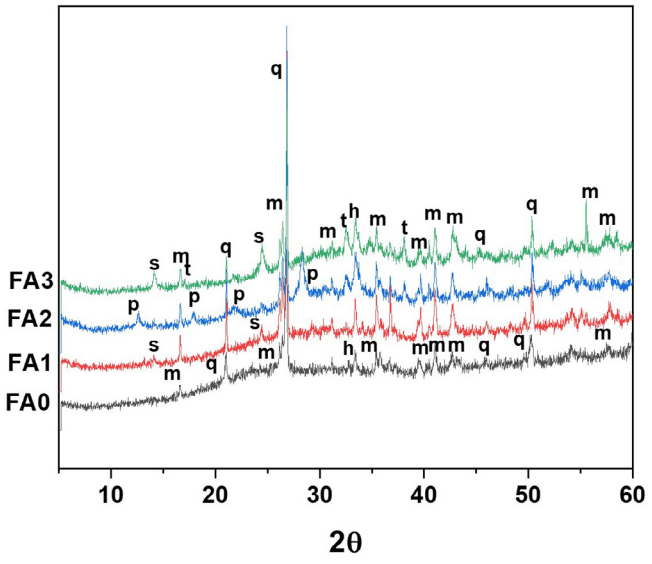

Fig. 3. XRD patterns of the samples. q: quartz, m: mullite, h: hematite, s: sodalite, p: zeolite P and t: thermonatrite.

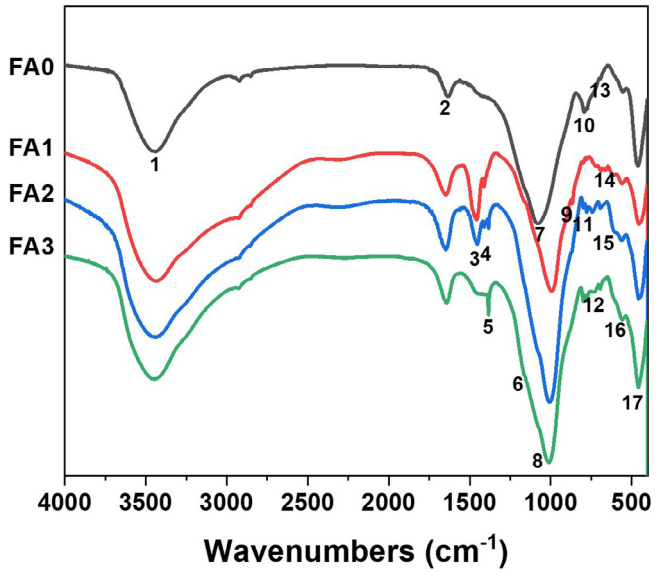

Fig. 4. FTIR spectra of the samples.

ascribed to the stretching vibration of Al-O bond, AlO_6) (Beran et al., 2001).

In the case of fly ash, FA0, the two intense and broad absorption bands (peaks 6 and 7 and peak 17) were attributed to the asymmetric stretching vibration of the T-O bonds (T = Si or Al) and bending vibration of O-Si-O bonds of internal TO_4 tetrahedra, respectively (Criado et al., 2016; Palomo et al., 2007; Zhang et al., 2018). The Al(Si)-O asymmetric stretching vibration band shifted from 1079 to 1006–994 cm^{-1} in the original fly ash towards lower frequencies, regarded as a peak of the formation of sodium aluminosilicate hydrate (N-A-S-H) gel. This position of the peak depended on the number of activations, which was located at higher frequencies with the increase of the activation number. It was indicated a higher Si content in the composition of the reaction products, in agreement with the XRD results, where zeolite P with Si/Al = 1.67 was formed after the second activation.

The formation of a Si-richer N-A-S-H gel after the third activation was consistent with the HF chemical attack results (see Fig. 2), according to which the percentage of reactive silica was always higher than that of reactive alumina concerning the potentially reactive phases. The alkaline activation of fly ashes is a process comprising the dissolution of starting materials and the formation of aluminosilicate gels (-Fernández-Jiménez et al., 2006a,b). The dissolution stage begins immediately after the alkaline solution comes into contact with the fly ash. In this stage, the high concentration of OH^- ions in the media breaks of covalent Si–O–Si, Si–O– Al, and Al–O–Al bonds present in the vitreous phase of the ash, releasing the silicon and aluminium ions into the solution and forming Si–OH and Al–OH groups. During the gelation stage, ionic species present in the solution condense to form Si–O–Al, and Si–O–Si bonds, giving rise to the formation of a three-dimensional aluminosilicate gel with alkaline cations compensating the deficit charges associated with Al for Si substitution. In the gelation stage, in the beginning, an N-A-S-H gel with a Si/Al ratio of around one is formed, but at the end of this stage the silica continues to incorporate in the medium and the reaction product presents a high silica content (Duxson et al., 2005c; Fernández-Jiménez et al., 2006b; Palomo et al., 2007). Both aspects were reflected by the shift in the T-O asymmetric stretching band toward higher frequencies, corroborated by SEM/EDX as well.

The FTIR spectra of the zeolites present two groups of vibrations (Flanigen et al., 1971; Ma and Lothenbach, 2020): a) internal vibration of the TO_4 tetrahedra (T = Si or Al), such as asymmetric stretching at 1250–920 cm^{-1}, symmetric stretching at 720–650 cm^{-1}, and T-O bending at 500–420 cm^{-1}. b) external vibrations of linkages, such as asymmetric stretching at 1150–1050 cm^{-1}, symmetric stretching at 820–750 cm^{-1}, ring vibrations at 650–500 cm^{-1}, and pore opening vibrations at 420–300 cm^{-1}. The presence of sodalite was confirmed by detection of the broad band at around 985 cm^{-1} (asymmetric stretching vibration of T-O-T bond, peak 8), the bands at around 726 and 664 cm^{-1} (symmetric stretching vibration of T-O-T, peaks 12 and 14), and the band at 457 cm^{-1} (peak 17), characteristics of bending vibration of O-T-O (Eterigho-Ikelegbe et al., 2020; Naskar et al., 2011).

When the fly ash was alkali-activated twice, FA2, the FTIR spectrum shows a series of peaks at 934 cm^{-1} (asymmetric stretching of T-O-T bond, peak 8), 741 cm^{-1} (external symmetric stretching of T-O-T bond, peak 11), 690 cm^{-1} (internal symmetric stretching of T-O-T bond, peak 13), 609 cm^{-1} (external ring, peak 15) and 456 cm^{-1} (bending of O-T-O, peak 17). All these bands indicated the formation of zeolite P (Ma and Lothenbach, 2020). The confirmation of the presence of these zeolites in the FTIR spectra after the different activation was in good agreement with the XRD data.

Finally, one band at around 1393 cm^{-1} (peak 5) was detected mainly after the second and the third activation, FA2 and FA3, it corresponded to stretching vibration of C-O, confirming the presence of carbonate groups, sodium carbonate, after these activations (Criado

Table 5
Bands on the FTIR spectra of the samples.

Band	Assigned to	FA0	FA1	FA2	FA3
1	Stret. O–H in water	3446	3433	3444	3446
2	Bend. H-O–H in water	1633	1646	1646	1633
3	Asym. stret. C-O in carbonates	1437	1458	1452	1453
4	Asym. stret. C-O in carbonates	–	1411	1412	–
5	Asym. stret. C-O in $Na_2CO_3{\cdot}H_2O$	–	1386	1383	1383
6	Asym. stret. Si-O-Si	1171	1171	1171	1171
7	Asym. stret. T-O bond (T = Si or Al) in anhydrous fly ash	1079	–	–	–
8	Asym. stret. T-O bond in N-A-S-H or (C)-N-A-S-H	–	994	1006	1010
9	Out-of-plane C-O in carbonates	–	866	870	–
10	Quartz band	794 & 774	798 & 778	798 & 778	798 & 778
11	Sym. stret. T-O Zeolite P	–	–	741	–
12	Sym. stret. T-O Sodalite	–	721	–	726
13	Quartz band	692	691	694	694
14	Sym. stret. T-O Sodalite	–	664	–	–
15	Ring external Zeolite P	–	–	609	–
16	Mullite band	553	560	560	556
17	Bend. O-Si-O	461	456	456	457

Bend. = bending, Asym. stret. = asymmetric stretching, Sym. stret. = symmetric stretching.

et al., 2005; Hamdane et al., 2020; Ortega-Zavala et al., 2019; Yuan et al., 2017). The formation of this type of carbonate after exposure to the atmosphere was supported by the XRD results.

Fig. 5 compares the microstructure of the alkali-activated specimens after the first, second, and third activation (FA1, FA2 and FA3). After the first activation, the micrograph FA1 showed the presence of the sodium aluminosilicate hydrate (N-A-S-H) gel, which constituted the cementitious material detected between partially or completely unreacted ash particles. The product had a relatively large number of small pores and some spherical coarser pores due to the partial or total reaction of fly ash particles. The gel growth took place on the surface of the spherical ash particles, acting as the initial nucleation points (Sindhunata et al., 2006). However, specific changes were detected in the reaction product after the second activation, the micrograph FA2 showed a denser and uniform matrix, whose appearance was similar to glass, with some isolated pores. Finally, after the third activation, FA3, the microstructure showed a more heterogeneous and discontinuous binder with a layered texture. Some reaction products were deposited about other ones. Nevertheless, the specimen FA3 exhibited a microstructure with a near absence of pores.

A higher resolution (x2000) was employed to find the average composition of the reaction products by EDX and to study in more detail the morphological characteristics of the three materials. Fig. 6a shows the morphological characteristics of the fly ash activated after the first activation, FA1. The main reaction product presented a Si/Al ratio of 1.41 and a Na/Al ratio of 0.65. Microstructural observations also revealed that there are crystalline deposits, usually found inside of the partially unreacted ash spheres or between particles, corresponding to the zeolites detected by XRD. Fig. 6b shows the presence of well-formed sodalite crystals with a Si/Al ratio of 1.35 and a Na/Al ratio of 0.45. Additionally, through Fig. 6c a series of needle-shaped crystals were also identified, which more than likely corresponded to NaOH supplied by the alkaline solution.

Fig. 7 shows the morphologic and microstructural characteristics of the ash activated after the second activation, FA2. The reaction product appeared like a monolayer of a glass, whose composition varied with respect to that formed after the first activation (FA1), Si/Al ratio of 2.16, and Na/Al ratio of 1.19. It seemed that the lower reactive alumina content in the medium induced the formation of an Al-poor aluminosilicate gel. These results agreed with those observed by FTIR, where a shift in the T-O asymmetric stretching band toward higher frequencies indicated a Si-enrichment of gel. The increase in Si/Al ratio results in a net increase in the volume of gel with an increase in bulk density as was observed in Table 6. These data are consistent with results reported by some authors (Duxson et al., 2005b), where greater lability of the silicate species within the sodium silicate activating solutions allows extensive gel reorganisation and densification, and facilitates pores to aggregate resulting in a microstructure comprising dense gel particles and large interconnecting pores, whereas reduced lability promotes a decreased localised gel density and distributed porosity.

In this system, the zeolitic crystals also appeared inside the pores or in the marks left by the fly ash that disappeared after the reaction. The crystalline morphology of these zeolites was more or less cubic, but as observed in the micrograph 9b, the cubes formed were not well defined, a longer curing time would be necessary for their crystalline development to be perfect. This zeolite had a Si/Al ratio of 1.75 and a Na/Al ratio of 1.04, with a composition that corresponds specifically to a zeolite P, detected by XRD.

Fig. 8 shows the morphologic and microstructural characteristics of the ash activated after the third activation, FA3. This micrograph revealed that there were phase heterogeneities showing regions of higher aluminium concentration (darker zones) and regions of higher sodium concentration (light zones). According to EDX analysis, the Si/Al and Na/Al ratios of the reaction product corresponding to the dark zone were 2.08 and 8.77, respectively, see Fig. 6b. While these ratios were 4.32 and 29.48 for the reaction product corresponding to the light zone, see Fig. 6c. With increasing Na content due to the successive activations to which the material was exposed, more Na was incorporated in the structure of the gel (Bhagath Singh and Subramaniam, 2017). In this case, it is worth noting that the amount of reactive alumina after the third activation could have been consumed in the first stage of reaction (dissolution) and therefore, the reaction products formed practically did not incorporate aluminium in its structure, but if a large amount of sodium supplied by the activating solution was. Part of Na present exists as change balancing cations in the three-dimensional aluminosilicate gel structure compensating the deficit charges associated with Al for Si substitution, while the remaining part exists partially associated in the form of $Na(H_2O)_n^+$ or within pore solution (Longhi et al., 2020; Walkley et al., 2018; Zhang et al., 2014). Therefore, a fraction of Na remains in excess, free and/or easily leachable generating more efflorescence and reducing the compressive strength of the material (see Fig. 12 and Table 6).

An outstanding fact concerning the system after the third activation, FA3, was the presence of sodium carbonate, as given in Fig. 9. Part of the sodium present in the system reacted with the atmospheric CO_2 producing sodium carbonate, confirming the formation of thermonatrite detected by XRD. However, the presence of zeolites was not observed probably due to the difficulty imposed by the layered morphology of the matrix.

Technological properties

The aspect of alkali-activated specimens can be observed in Fig. 10. Activated specimens from the original fly ash were grey (FA1) and dimensionally stable. However, once the specimens are grounded and reactivated, the new specimens (FA2) become a little bit darker, some black spots appear (note that they are not pores) and the specimens are slightly deformed. Finally, after the third activation (FA3), specimens become black, and several dimensional defects appear (warpage). This behaviour may be explained by the fact that with the successive activations a higher l/s ratio is required for shaping the

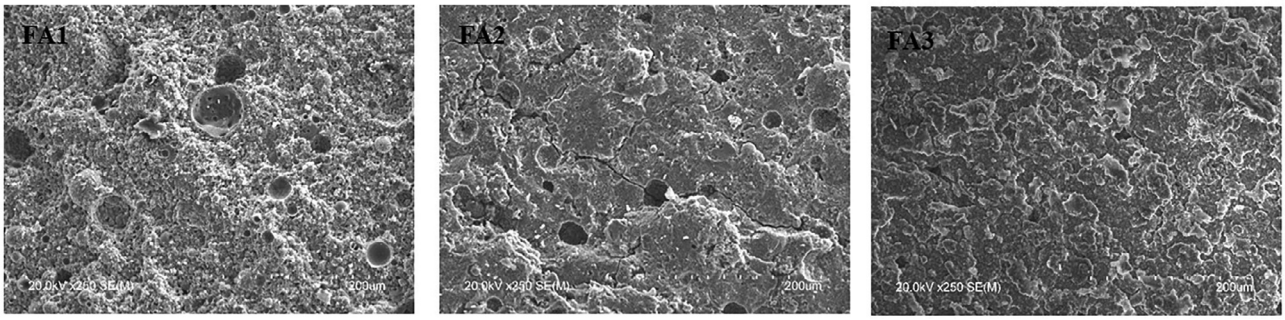

Fig. 5. General view of the alkali-activated fly ashes after the first, second, and third activation, (FA1, FA2 and FA) (x250).

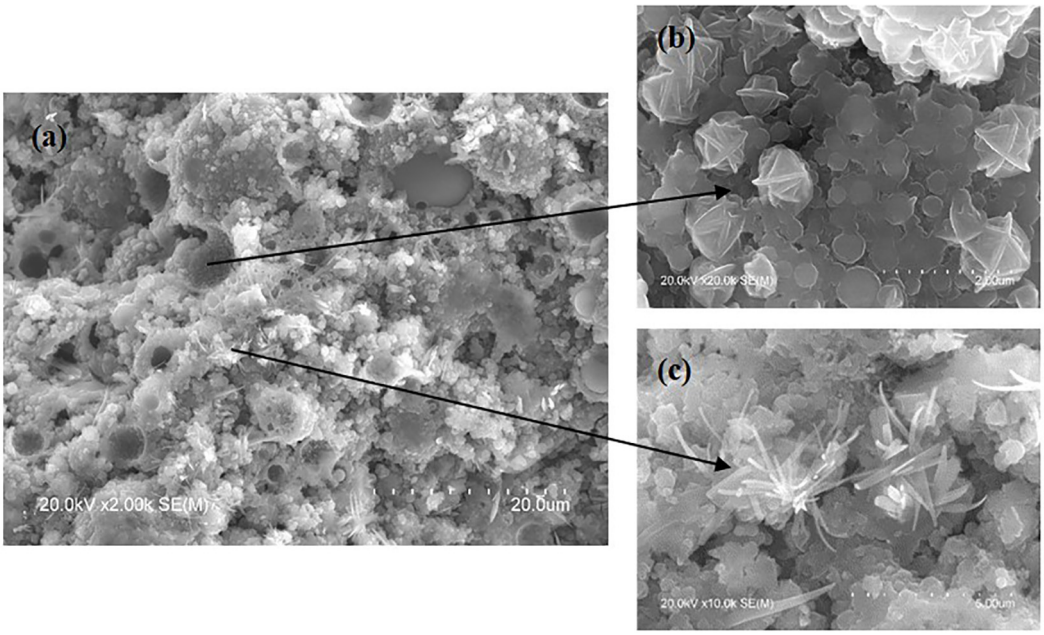

Fig. 6. Alkali-activated fly ash after the first activation, FA1 (x2k) (a); sodalite crystals (x20k) (b); and NaOH needles (x20k) (c).

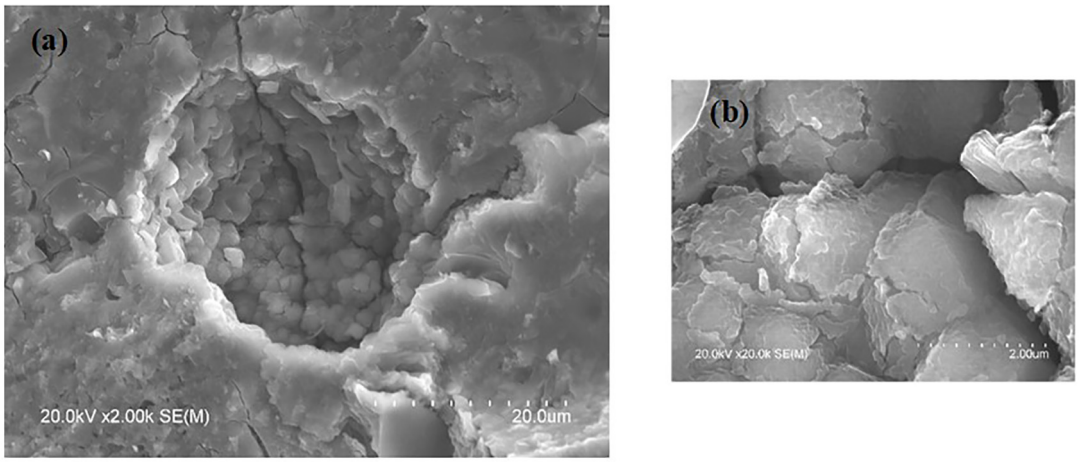

Fig. 7. Alkali-activated fly ash after the second activation, FA2 (x2k) (a); and zeolite P crystals (x20k) (b).

Table 6
Bulk density, mechanical strength and water absorption of samples after successive activations.

Specimen references	l/s ratio	Bulk density (g/cm^3)	Flexural strength (MPa)	Water absorption (%)
FA1	0.40	1.65 ± 0.01	9.2 ± 0.4	15.7 ± 1.0
FA2	0.43	1.81 ± 0.01	4.1 ± 0.2	10.7 ± 0.9
FA3	0.55	1.90 ± 0.01	0.2 ± 0.1	–

specimens, together with a lower content of reactive silica and alumina that produce an excess of alkaline solutions that makes the specimens more deformable during the demoulding.

Table 6 shows the values of bulk density, bending strength and water absorption after maintaining all specimens 24 h at room conditions once the curing stage was finished. Bulk density increases and open porosity (water absorption) decreases when successive activations were carried out. This difference can possibly be due to the fact that the original fly ash has a narrower particle size distribution (higher reject value) while the powders obtained after several activations have an increasingly wider particle size distribution (lower reject value); therefore, reactivated powders pack better and result in specimens with higher bulk density and lower water absorption (both properties are usually paired together, better packing reduces porosity).

Another explanation could be the formed gel in the previous activations does not dissolve during successive activations and thus acts as a filler, and therefore does improve the packaging. However, this hypothesis cannot be supported by the literature.

After all, other authors (Duxson et al., 2005b) have observed this same effect and have attributed it to the fact that the increase of liq-

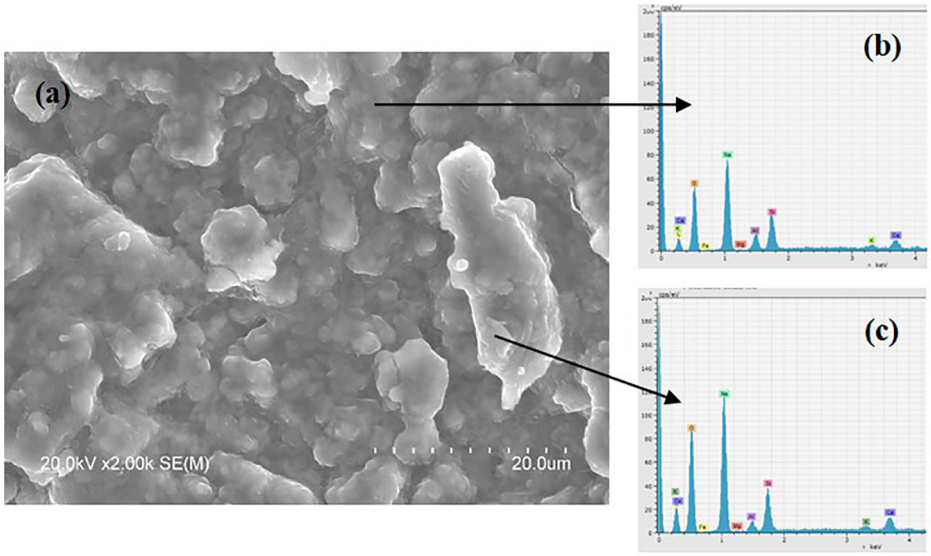

Fig. 8. Alkali-activated fly ash after the third activation, FA3 (x2k) (a); elemental analysis of the reaction product corresponding to the dark region (b); and elemental analysis of the reaction product corresponding to the light region.

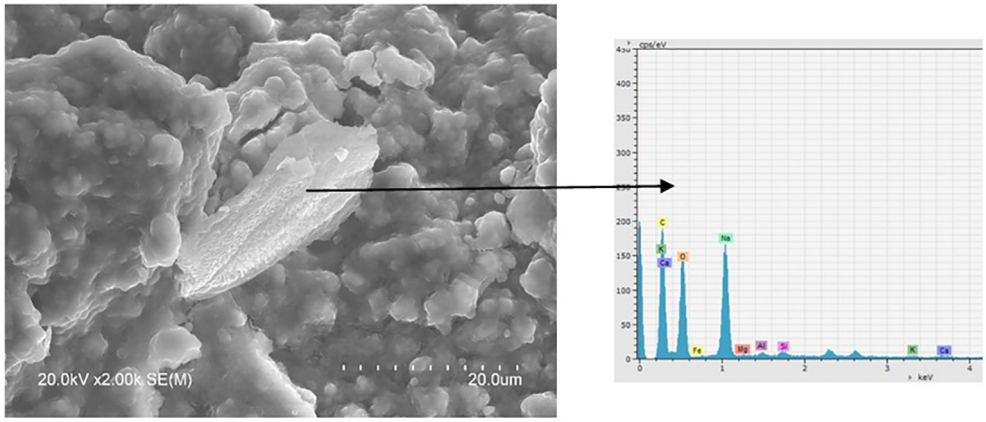

Fig. 9. Crystals of sodium carbonate detected after the third alkaline activation of fly ash.

uid/solid ratio, in other words, the increase of alkaline activator, leads to an amount of silicate, concluding that greater lability of silicate species promotes a reorganisation and densification of gel.

Regarding bending strength, it is observed that the value obtained from the specimens prepared with the original fly ash was around 9 MPa. After the first reactivation, the flexural strength decreased to just under half and in the last activation, it was hardly any strength. This behaviour could possibly be due to the carbonation of the aluminosilicate powders (FA1 powder to prepare FA2 specimens and FA2 powder to prepare FA3 specimens). Another cause could be the formed gel in the previous activations does not dissolve during successive activations and thus acts as a filler, and therefore less binder is formed. However, this hypothesis cannot be supported by the literature, as explained above. Therefore, there are other factors to be taken into account and they are explained as follows.

An improvement in microstructural homogeneity provides strong reasoning for the increase in mechanical properties since Si-O-Al and Al-O-Al bonds are weaker than Si-O-Si linkages, meaning that the strength of alkali-activated samples should increase with the Si/Al ratio since the density of Si-O-Si linkages increases with this ratio (Duxson et al., 2005a,b), but the decrease in mechanical strength of specimens obtained after the second and third activation with higher

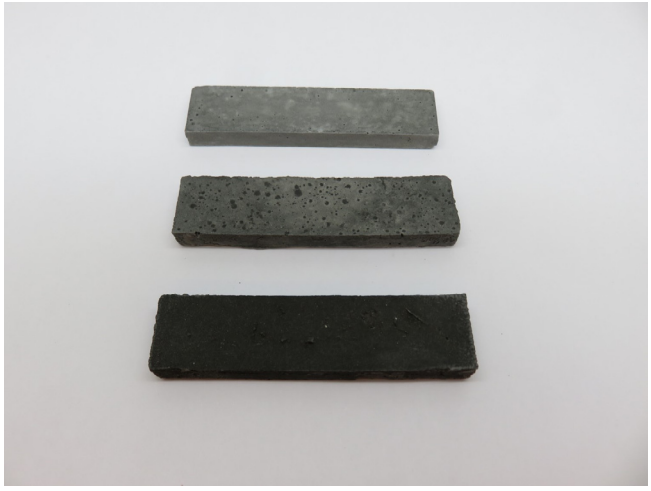

Fig. 10. Aspect of the alkali-activated specimens.

Si/Al ratios suggests that other factors must affect the mechanical properties.

The rate of dissolution of ashes strongly depends on the amount and composition of ashes, for example, the potentially reactive silica and alumina. In this study, the reactive silica content is likewise similar, but the reactive alumina content differs and decreases appreciably after each activation. After the third activation, the most reactive alumina has been consumed in the dissolution stage and the reaction product contains low Si and Al, but a high percentage of Na. Fernández-Jiménez et al. (Fernández-Jiménez et al., 2006b) and Xu et al. (Xu and Van Deventer, 2000) reported the existence of a correlation between the quantities of Si and Al dissolved in the reactional medium, synchronous dissolution of both elements, where a certain minimum amount of reactive Al is always necessary to favour the formation of aluminosilicate gels. The reactive Al absence after the third activation implies that the reactive silica dissolution speed is drastically reduced in the gelation stage and therefore, the composition of the reaction product has suffered modifications, decreasing the quantities of Si and Al in its structure.

The effect of minority elements in the fly ash such as alkalis, calcium, titanium, or iron must be also taken into consideration. In aluminosilicate glasses, alkali metals (mainly Na and K) and alkali earth metals (mainly Ca and Mg) can act as network modifiers, forming non-bridging oxygen sites (Fernández-Jiménez et al., 2019; Stebbins and Xu, 1997; Zhang et al., 2016) thus potentially reducing the degree of polymerisation of the aluminosilicate glasses if present at high enough concentrations. According to this idea, the Na enrichment of the aluminosilicate gel implies an increase in the number of non-bridging oxygen sites, which provide a relatively weak connection between one tetrahedral cation (Al or Si) and network modifier cation (Na^+) no forming an integral part of the tetrahedral network and leading a reduction of the mechanical strength. Therefore, another factor to consider when explaining mechanical strength development by the system is the structure and composition of the gel formed as the main reaction product.

Determination of the tendency to efflorescence formation

Fig. 11 shows the arrangement of the specimens during the test, part of them immersed in water and part of them exposed to the air. Due to the preferential drying in the upper part of the specimens, there is a concentration of the salts causing efflorescence development.

Fig. 12 shows the specimens FA1, FA2 and FA3 after 7 days of testing. FA3 specimens broke themselves during the test due to their low mechanical properties and therefore was not possible to evaluate its efflorescence formation. FA1 and FA2 specimens were tested, and in both cases, salt deposits were observed. It would be expected that more efflorescence would be present in FA2 specimens than in the FA1 ones; however, as the test is qualitative no big differences were observed.

The presence of efflorescence usually indicates the existence of an excess of alkaline solution, which has not reacted to form part of the structure of the alkali-activated product formed. In the following, an attempt is presented in order to explain why a little more efflorescence should appear in FA2.

Efflorescence of alkali-activated materials is a phenomenon that occurs due to the movement of free alkali through the pore network to the surface and reaction with the carbon dioxide from the environment under certain humidity conditions (mainly, when contact with water), forming typically sodium or potassium carbonates that crystallise on the specimen's surface and precipitate (Longhi et al., 2020). Therefore, systems in which only sodium hydroxide was used as an alkaline source show the most severe efflorescence although systems with an excess of sodium in the alkaline activator also show the presence of efflorescence, and maybe that is happening in the specimens shown in this work.

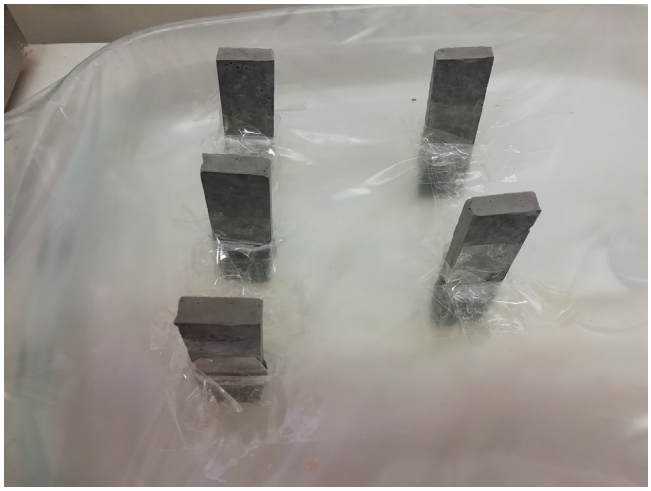

Fig. 11. Specimens disposed to determine the tendency to efflorescence formation (time: initial).

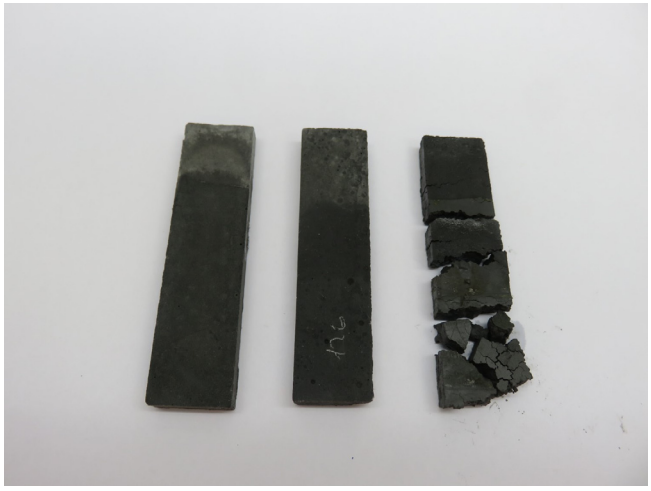

Fig. 12. Specimens obtained after the efflorescence test (time: 7 days).

The high content of alkalis used during activation can result in the removal of alkalis from both the pore network and gel framework and affect the geopolymer service life aesthetically due to the visual efflorescence formation or superficial deterioration and even could affect mechanically due to the reduction in compressive strength.

Conclusions

This work deals with the reactivation process of already alkali-activated materials with the aim of finding out the feasibility of valorising them at the end of their service life as starting materials to obtain new alkali-activated products.

It has been observed that the reactivation of already alkali-activated materials requires higher liquid/solid ratios to reach the right consistency for the forming of the specimens by casting. Successive alkaline activations provide the specimens with lower porosity, but with lower mechanical properties, reaching almost zero strength by the third activation.

The reasons why a loss of mechanical properties is observed with the successive activations are the lower reactive alumina content of the powder used as raw material and the formation of an alkaline aluminosilicate hydrate gel with more sodium in its structure, with a

weak connection between one tetrahedral cation (Al or Si) and network modifier cation (Na^+).

These results highlight, for the case of studied fly ash, its suitability for being used in a second activation, contributing to the sustainability of the construction materials.

Declaration of Competing Interest

The authors declare that they have no known competing financial interests or personal relationships that could have appeared to influence the work reported in this paper.

Acknowledgements

The work has been carried out thanks to 3 projects:

- CerOh! project supported by the Autonomous Government of Valencia (GVA), through the Valencian Institute for Business Competitiveness (IVACE) by its Nominative Line for 2020 and 2021 and by the European Regional Development Fund (ERDF) (references: IMDEEA/2018/12, IMDEEA/2019/5, IMAMCA/2020/1 and IMAMCA/2021/1).
- LIFE HYPOBRICK project funded by the European Union Environment and Climate Action Programme LIFE 2014-2020 (reference: LIFE18 CCM/ES/001114). It is also supported by IVACE of GVA.
- IRINEMAproject financially supported by the Community of Madrid through “Ayudas a la Atracción de Talento Investigador” (reference: 2019-T1/AMB-13672).

References

Ahmaruzzaman, M., 2010. A review on the utilization of fly ash. Prog. Energy Combust. Sci. 36 (3), 327–363. https://doi.org/10.1016/j.pecs.2009.11.003.

Beran, A., Voll, D., Schneider, H., 2001. Dehydration and structural development of mullite precursors: An FTIR spectroscopic study. J. Eur. Ceram. Soc. 21 (14), 2479–2485. https://doi.org/10.1016/S0955-2219(01)00265-5.

Bhagath Singh, G.V.P., Subramaniam, K.V.L., 2017. Evaluation of sodium content and sodium hydroxide molarity on compressive strength of alkali activated low-calcium fly ash. Cem. Concr. Compos. 81, 122–132. https://doi.org/10.1016/j.cemconcomp.2017.05.001.

Buchwald, A., Vicent, M., Kriegel, R., Kaps, C., Monzó, M., Barba, A., 2009. Geopolymeric binders with different fine fillers - Phase transformations at high temperatures. Appl. Clay Sci. 46 (2), 190–195. https://doi.org/10.1016/j.clay.2009.08.002.

Chi, M., 2015. Effects of modulus ratio and dosage of alkali-activated solution on the properties and micro-structural characteristics of alkali-activated fly ash mortars. Constr. Build. Mater. 99, 128–136. https://doi.org/10.1016/j.conbuildmat.2015.09.029.

Criado, M., Aperador, W., Sobrados, I., 2016. Microstructural and mechanical properties of alkali activated Colombian raw materials. Materials (Basel). 9, 1–16. https://doi.org/10.3390/ma9030158.

Criado, M., Fernández-Jiménez, A., de la Torre, A.G., Aranda, M.A.G., Palomo, A., 2007. An XRD study of the effect of the SiO2/Na2O ratio on the alkali activation of fly ash. Cem. Concr. Res. 37 (5), 671–679. https://doi.org/10.1016/j.cemconres.2007.01.013.

Criado, M., Palomo, A., Fernandezjimenez, A., 2005. Alkali activation of fly ashes. Part 1: Effect of curing conditions on the carbonation of the reaction products. Fuel 84 (16), 2048–2054. https://doi.org/10.1016/j.fuel.2005.03.030.

Darmayanti, L., Kadja, G.T.M., Notodarmojo, S., Damanhuri, E., Mukti, R.R., 2019. Structural alteration within fly ash-based geopolymers governing the adsorption of Cu2+ from aqueous environment: Effect of alkali activation. J. Hazard. Mater. 377, 305–314. https://doi.org/10.1016/j.jhazmat.2019.05.086.

Diaz-Loya, E.I., Allouche, E.N., Vaidya, S., 2011. Mechanical properties of fly-ash-based geopolymer concrete. ACI Mater. J. 108, 300–306. https://doi.org/10.14359/51682495.

Duxson, P., Lukey, G.C., Van De Venter, J.S., Mallicoat, S.W., Kriven, W.M., 2005a. Microstructural characterisation of metakaolin-based geopolymers. Ceram. Trans. 165, 71–85. https://doi.org/10.1002/9781118408353.ch7.

Duxson, P., Provis, J.L., Lukey, G.C., Mallicoat, S.W., Kriven, W.M., van Deventer, J.S.J., 2005b. Understanding the relationship between geopolymer composition, microstructure and mechanical properties. Colloids Surfaces A Physicochem. Eng. Asp. 269 (1-3), 47–58. https://doi.org/10.1016/j.colsurfa.2005.06.060.

Duxson, P., Provis, J.L., Lukey, G.C., Separovic, F., van Deventer, J.S.J., 2005c. 29Si NMR study of structural ordering in aluminosilicate geopolymer gels. Langmuir 21 (7), 3028–3036. https://doi.org/10.1021/la047336x.

EN 450-1:2006 + A1:2008. Fly ash for concrete - Part 1: Definition, specifications and conformity criteria., n.d,

Eterigho-Ikelegbe, O., Bada, S., Daramola, M.O., Falcon, R., 2020. Synthesis of high purity hydroxy sodalite nanoparticles via pore-plugging hydrothermal method for inorganic membrane development: Effect of synthesis variables on crystallinity, crystal size and morphology. Mater. Today Proc. 10.1016/j.matpr.2020.03.693.

European Commission. Eurostat. Manuals and Guidelines.Circular material use rate CALCULATION METHOD 2018 edition [WWW Document], 2018. URL https://ec.europa.eu/eurostat/documents/3859598/9407565/KS-FT-18-009-EN-N.pdf/b8efd42b-b1b8-41ea-aaa0-45e127ad2e3f (accessed 8.13.21).

European Commission. Eurostat. Products Datasets [WWW Document], 2021. URL https://ec.europa.eu/eurostat/web/products-datasets/-/cei_srm030 (accessed 8.13.21).

Fernández-Jiménez, A., Garcia-Lodeiro, I., Maltseva, O., Palomo, A., 2019. Mechanical-chemical activation of coal fly ashes: An effective way for recycling and make cementitious materials. Front. Mater. 6, 1–12. https://doi.org/10.3389/fmats.2019.00051.

Fernández-Jiménez, A., Monzó, M., Vicent, M., Barba, A., Palomo, A., 2008. Alkaline activation of metakaolin-fly ash mixtures: Obtain of Zeoceramics and Zeocements. Microporous Mesoporous Mater. 108 (1-3), 41–49. https://doi.org/10.1016/j.micromeso.2007.03.024.

Fernández-Jiménez, A., Palomo, A., Criado, M., 2006a. Activación alcalina de cenizas volantes. Estudio comparativo entre activadores sódicos y potásicos. Mater. Constr. 56, 51–65. https://doi.org/10.3989/mc.2006.v56.i281.92.

Fernández-Jiménez, A., Palomo, A., Criado, M., 2005. Microstructure development of alkali-activated fly ash cement: A descriptive model. Cem. Concr. Res. 35 (6), 1204–1209. https://doi.org/10.1016/j.cemconres.2004.08.021.

Fernández-Jiménez, A., Palomo, A., Sobrados, I., Sanz, J., 2006b. The role played by the reactive alumina content in the alkaline activation of fly ashes. Microporous Mesoporous Mater. 91 (1-3), 111–119. https://doi.org/10.1016/j.micromeso.2005.11.015.

Flanigen, E.M., Khatami, H., Szymanski, H.A., 1971. Infrared structural studies of zeolite frameworks., in: Flanigen, Edith M, Sand, L.B. (Ed.), Molecular Sieve Zeolites-I. ACS Publications, pp. 201–229. 10.1021/ba-1971-0101

Gikunoo, E., Omotoso, O., Oguocha, I.N.A., 2005. Effect of fly ash particles on the mechanical properties of aluminium casting alloy A535. Mater. Sci. Technol. 21 (2), 143–152. https://doi.org/10.1179/174328405X18601.

Hamdane, H., Tamraoui, Y., Mansouri, S., Oumam, M., Bouih, A., El Ghailassi, T., Boulif, R., Manoun, B., Hannache, H., 2020. Effect of alkali-mixed content and thermally untreated phosphate sludge dosages on some properties of metakaolin based geopolymer material. Mater. Chem. Phys. 248, 122938. https://doi.org/10.1016/j.matchemphys.2020.122938.

Harris, D., Heidrich, C., Feuerborn, J., 2019. Global aspects on Coal Combustion Products. VGB Power tech, 25–33.

Husaini, S.N., Khan, E.U., Khattak, N.U., Qureshi, A.A., Malik, F., Qureshi, I.E., Karim, T., Khan, H.A., 2002. The study of crystalline etch products of CR-39. Radiat. Meas. 35 (1), 3–5. https://doi.org/10.1016/S1350-4487(01)00259-1.

Longhi, M.A., Rodríguez, E.D., Walkley, B., Zhang, Z., Kirchheim, A.P., 2020. Metakaolin-based geopolymers: Relation between formulation, physicochemical properties and efflorescence formation. Compos. Part B Eng. 182, 107671.

Ma, B., Lothenbach, B., 2020. Cement and Concrete Research Synthesis, characterization, and thermodynamic study of selected Na-based zeolites. Cem. Concr. Res. 135, 106111. https://doi.org/10.1016/j.cemconres.2020.106111.

Ma, Y., Ye, G., Hu, J., 2017. Micro-mechanical properties of alkali-activated fly ash evaluated by nanoindentation. Constr. Build. Mater. 147, 407–416. https://doi.org/10.1016/j.conbuildmat.2017.04.176.

Mardani-Aghabaglou, A., Inan Sezer, G., Ramyar, K., 2014. Comparison of fly ash, silica fume and metakaolin from mechanical properties and durability performance of mortar mixtures view point. Constr. Build. Mater. 70, 17–25. https://doi.org/10.1016/j.conbuildmat.2014.07.089.

Mobili, A., Telesca, A., Marroccoli, M., Tittarelli, F., 2020. Calcium sulfoaluminate and alkali-activated fly ash cements as alternative to Portland cement: study on chemical, physical-mechanical, and durability properties of mortars with the same strength class. Constr. Build. Mater. 246, 118436. https://doi.org/10.1016/j.conbuildmat.2020.118436.

Naskar, M.K., Kundu, D., Chatterjee, M., 2011. Effect of process parameters on surfactant-based synthesis of Hydroxy sodalite particles. Mater. Lett. 65 (3), 436–438. https://doi.org/10.1016/j.matlet.2010.11.008.

Ortega-Zavala, D.E., Santana-Carrillo, J.L., Burciaga-Díaz, O., Escalante-García, J.I., 2019. An initial study on alkali activated limestone binders. Cem. Concr. Res. 120, 267–278. https://doi.org/10.1016/j.cemconres.2019.04.002.

Ouda, A.S., Gharieb, M., 2021. Behavior of alkali-activated pozzocrete-fly ash paste modified with ceramic tile waste against elevated temperatures and seawater attacks. Constr. Build. Mater. 285, 122866. https://doi.org/10.1016/j.conbuildmat.2021.122866.

Palomo, A., Criado, M., Fernández-Jiménez, A., 2007. Alkali activation of fly ash : Effect of the SiO2/Na2O ratio Part I : FTIR study. Microporous Mesoporous Mater. 106, 180–191. https://doi.org/10.1016/j.micromeso.2007.02.055.

Palomo, A., Grutzeck, M.W., Blanco, M.T., 1999. Alkali-activated fly ashes: A cement for the future. Cem. Concr. Res. 29 (8), 1323–1329. https://doi.org/10.1016/S0008-8846(98)00243-9.

Rogoff, M.J., Screve, F., 2019. Waste-to-energy: technologies and project implementation. Academic Press.

Ruengsillapanun, K., Udtaranakron, T., Pulngern, T., Tangchirapat, W., Jaturapitakkul, C., 2021. Mechanical properties, shrinkage, and heat evolution of alkali activated fly ash concrete. Constr. Build. Mater. 299, 123954. https://doi.org/10.1016/j.conbuildmat.2021.123954.

Sánchez, E., García-Ten, J., Barba, A., Beltrán, V., 1998. Estimation of packing density of raw material mixtures used in tile manufacture. Br. Ceram. Trans. 97, 149–154.
Sindhunata, van Deventer, J.S.J., Lukey, G.C., Xu, H., 2006. Effect of curing temperature and silicate concentration on fly-ash-based geopolymerization. Ind. Eng. Chem. Res. 45 (10), 3559–3568. https://doi.org/10.1021/ie051251p.
Škvára, F., Kopecký, L., Šmilauer, V., Bittnar, Z., 2009. Material and structural characterization of alkali activated low-calcium brown coal fly ash. J. Hazard. Mater. 168 (2-3), 711–720. https://doi.org/10.1016/j.jhazmat.2009.02.089.
Stebbins, J.F., Xu, Z., 1997. NMR evidence for excess non-bridging oxygen in an aluminosilicate glass. Nature 390 (6655), 60–62. https://doi.org/10.1038/36312.
UNE 80225, 2012. Métodos de ensayo de cementos. Análisis químico. Determinación del dióxido de silicio (SiO2) reactivo en los cementos, en las puzolanas y en las cenizas volantes. AENOR, Madrid, Spain.
Van Bekkum, H., Flanigen, E.M., Jacobs, P.A., Jansen, J.C., 2001. Introduction to zeolite science and practice, 2nd. Studies in surface science and catalysis, Elsevier, Amsterdam, The Netherlands.
Vu, T.H., Gowripalan, N., 2018. Mechanisms of heavy metal immobilisation using geopolymerisation techniques – A review. J. Adv. Concr. Technol. 16 (3), 124–135. https://doi.org/10.3151/jact.16.124.
Walkley, B., Rees, G.J., San Nicolas, R., van Deventer, J.S.J., Hanna, J.V., Provis, J.L., 2018. New Structural Model of Hydrous Sodium Aluminosilicate Gels and the Role of Charge-Balancing Extra-Framework Al. J. Phys. Chem. C 122 (10), 5673–5685. https://doi.org/10.1021/acs.jpcc.8b0025910.1021/acs.jpcc.8b00259.s001.
Xia, M., Muhammad, F., Zeng, L., Li, S., Huang, X., Jiao, B., Shiau, Y.C., Li, D., 2019. Solidification/stabilization of lead-zinc smelting slag in composite based geopolymer. J. Clean. Prod. 209, 1206–1215. https://doi.org/10.1016/j.jclepro.2018.10.265.
Xiao, R., Jiang, X.i., Wang, Y., He, Q., Huang, B., 2021. Experimental and Thermodynamic Study of Alkali-Activated Waste Glass and Calcium Sulfoaluminate Cement Blends: Shrinkage, Efflorescence Potential, and Phase Assemblages. J. Mater. Civ. Eng. 33 (11), 04021312.
Xiao, R., Jiang, X., Zhang, M., Polaczyk, P., Huang, B., 2020. Analytical investigation of phase assemblages of alkali-activated materials in CaO-SiO2-Al2O3 systems: The management of reaction products and designing of precursors. Mater. Des. 194,. https://doi.org/10.1016/j.matdes.2020.108975 108975.
Xu, H., Van Deventer, J.S.J., 2000. The geopolymerisation of alumino-silicate minerals. Int. J. Miner. Process. 59, 247–266. https://doi.org/10.1016/S0301-7516(99)00074-5.
Yousefi Oderji, S., Chen, B., Ahmad, M.R., Shah, S.F.A., 2019. Fresh and hardened properties of one-part fly ash-based geopolymer binders cured at room temperature: Effect of slag and alkali activators. J. Clean. Prod. 225, 1–10. https://doi.org/10.1016/j.jclepro.2019.03.290.
Yuan, B., Yu, Q.L., Brouwers, H.J.H., 2017. Time-dependent characterization of Na 2 CO 3 activated slag. Cem. Concr. Compos. 84, 188–197.
Zerzouri Lakhssassi, M., Alehyen, S., El Alouani, M., Taibi, M., 2019. The effect of aggressive environments on the properties of a low calcium fly ash based geopolymer and the ordinary Portland cement pastes. Mater. Today:. Proc. 13, 1169–1177. https://doi.org/10.1016/j.matpr.2019.04.085.
Zhang, Z., Provis, J.L., Ma, X., Reid, A., Wang, H., 2018. Efflorescence and subflorescence induced microstructural and mechanical evolution in fly ash-based geopolymers. Cem. Concr. Compos. 92, 165–177. https://doi.org/10.1016/j.cemconcomp.2018.06.010.
Zhang, Z., Provis, J.L., Reid, A., Wang, H., 2014. Fly ash-based geopolymers: The relationship between composition, pore structure and efflorescence. Cem. Concr. Res. 64, 30–41. https://doi.org/10.1016/j.cemconres.2014.06.004.
Zhang, Z., Provis, J.L., Zou, J., Reid, A., Wang, H., 2016. Toward an indexing approach to evaluate fly ashes for geopolymer manufacture. Cem. Concr. Res. 85, 163–173. https://doi.org/10.1016/j.cemconres.2016.04.007.
Environment Action Programme to 2020. Environment Policies. Waste [WWW Document], 2020. URL http://ec.europa.eu/environment/waste/index.htm (accessed 8.13.21).